

Above-bandgap magneto-optical Kerr effect in ferromagnetic Ga_{1-x}Mn_xAsC. Sun,^{1,2,3} J. Kono,^{1,2,3,*} Y.-H. Cho,⁴ A. K. Wójcik,⁴ A. Belyanin,⁴ and H. Munekata⁵¹*Department of Electrical and Computer Engineering, Rice University, Houston, Texas 77005, USA*²*Department of Physics and Astronomy, Rice University, Houston, Texas 77005, USA*³*The Richard E. Smalley Institute for Nanoscale Science and Technology, Rice University, Houston, Texas 77005, USA*⁴*Department of Physics, Texas A&M University, College Station, Texas 77843, USA*⁵*Imaging Science and Engineering Laboratory, Tokyo Institute of Technology, Yokohama, Kanagawa 226-8503, Japan*

(Received 19 May 2010; revised manuscript received 4 February 2011; published 25 March 2011)

We performed a systematic magneto-optical Kerr spectroscopy study of Ga_{1-x}Mn_xAs with varying Mn densities as a function of temperature, magnetic field, and photon energy. Unlike previous studies, the magnetization easy axis was perpendicular to the sample surface, allowing us to take remanent polar Kerr spectra in the absence of an external magnetic field. The remanent Kerr angle strongly depended on the photon energy, exhibiting a large positive peak at ~ 1.7 eV. This peak increased in intensity and blueshifted with Mn doping and further blueshifted with annealing. Using a 30-band $\mathbf{k} \cdot \mathbf{p}$ model with antiferromagnetic s, p - d exchange interaction, we calculated the dielectric tensor of Ga_{1-x}Mn_xAs in the interband transition region, assuming that our samples are in the metallic regime and the impurity band has merged with the valence band. Our modeling successfully reproduces the observed spectra.

DOI: [10.1103/PhysRevB.83.125206](https://doi.org/10.1103/PhysRevB.83.125206)

PACS number(s): 78.67.Ch, 71.35.Ji, 78.55.-m

I. INTRODUCTION

Dilute magnetic semiconductors,¹ i.e., II–VI or III–V semiconductors doped with transition-metal ions, show a variety of magnetic phenomena arising from the interplay between localized and delocalized carriers. The strong s, p - d exchange interaction between band carriers (s, p) and Mn local moments (d) results in enormous enhancement of carrier g factors as well as the formation of magnetic polarons. The discovery of carrier-induced ferromagnetism in (III,Mn)V semiconductors^{2–5} with relatively high Curie temperatures ($T_c < 190$ K)⁶ has stimulated further interest in these systems from both applied and fundamental viewpoints.⁷ Although it has been experimentally established that the ferromagnetic interaction between Mn moments is mediated by free holes,^{8,9} there remain some basic questions as to the nature of the free holes (p -like or d -like) and the role of Mn impurity bands in transport and optical processes.

Magneto-optical (MO) spectroscopy is useful for studying spin-dependent electronic states in magnetic systems via polarization-dependent reflection and absorption, i.e., the MO Kerr effect (MOKE) and magnetic circular dichroism (MCD). Previous MO studies of Ga_{1-x}Mn_xAs,^{10–22} however, have produced much controversy regarding the value and sign of the p - d exchange coupling constant, J_{pd} , the position of the Fermi level, the insulating versus metallic nature of the samples, and the contribution of the optical transitions originated from Mn impurity states.

One of the commonly observed characteristics in MO spectra for ferromagnetic Ga_{1-x}Mn_xAs is that the sign of the MO signal above the band gap (~ 1.4 to ~ 2 eV) corresponds to greater absorption for σ^- polarization of light than for σ^+ polarization, which is opposite to (II,Mn)VI systems¹ as well as paramagnetic Ga_{1-x}Mn_xAs with low Mn doping. An opposite sign of MO signal could indicate an opposite sign of exchange coupling. Szczytko *et al.*¹¹ proposed that the sign difference is a result of E_F being inside the valence

band in ferromagnetic Ga_{1-x}Mn_xAs while p - d exchange coupling is still antiferromagnetic ($J_{pd} > 0$) as in (II,Mn)VI; due to exchange splitting, the Moss-Burstein shift²³ is expected to become spin dependent and thus the lowest-energy σ^+ transition should occur at a large momentum, while the lowest-energy σ^- transition should still occur near the zone center. Komori *et al.* also explained their MO data by adopting this model.¹⁴ However, Lang *et al.*,¹⁸ in analyzing their MO data within a parabolic band model assuming that E_F resides inside the valence band, had to conclude that p - d exchange coupling is ferromagnetic ($J_{pd} < 0$); to explain their data quantitatively, they were also forced to introduce a dispersionless level of unclear origin inside the conduction band that would need to have a very large oscillator strength (three times larger than the usual valence-band-to-conduction-band transitions). To identify the optical contribution from the impurity band, infrared spectroscopy studies were carried out as it probes electronic states near the Fermi surface. Burch *et al.*^{16,17} interpreted the observed peak around 0.2 eV as the valence-band-to-impurity-band transition. On the contrary, Acbas *et al.*²² measured infrared Kerr and Faraday effects in Ga_{1-x}Mn_xAs and explained the spectra with a valence-band-hole theory.

Tang and Flatté²⁴ modeled the MCD in Ga_{1-x}Mn_xAs and concluded that the transitions between the impurity band and the bulk bands play a dominant role. Further theoretical MCD studies using a similar approach²⁵ came to the conclusion that an agreement with experiment is possible both with and without an impurity band included in the modeling. In addition, Ando *et al.*²⁰ and Berciu *et al.*²¹ both performed a MCD study on paramagnetic and low- T_c ferromagnetic Ga_{1-x}Mn_xAs samples. Ando *et al.* claimed that the MO features below 1.4 eV are likely to be related to impurity states. They interpreted their above-bandgap spectra in ferromagnetic samples as being composed of a broad positive impurity-related background and negative and positive peaks associated

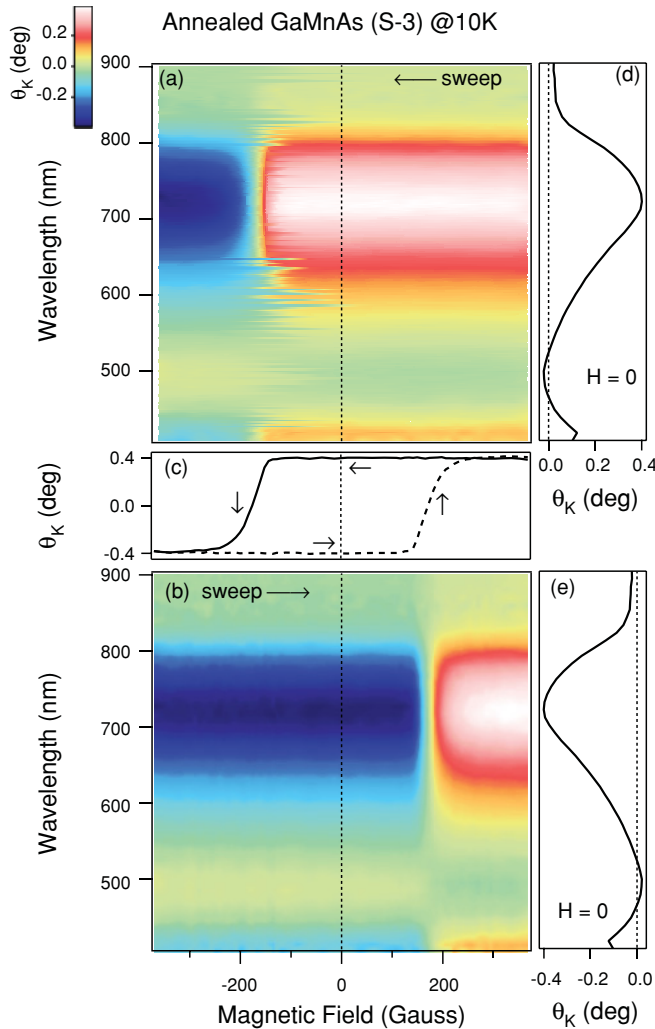


FIG. 1. (Color online) Contour plot of the measured Kerr angle as a function of magnetic field and wavelength for an annealed $\text{Ga}_{0.976}\text{Mn}_{0.024}\text{As}$ (S-3) at 10 K. Magnetic field was (a) swept from +400 to -400 G and (b) reversed. (c) A hysteresis loop with magnetic field swept from +400 to -400 G (solid line) and from -400 to +400 G (dashed line). (d) and (e) Wavelength dependence of remanent Kerr angle (i.e., no external magnetic field) for down-sweep and up-sweep, respectively.

with band-edge singularities (E_0 and $E_0 + \Delta_0$ critical points, respectively), concluding that E_F is in the Mn impurity band and there is no Moss-Burstein shift. Berciu *et al.*, based on their sample-dependent analysis and simplified one-dimensional model, proposed a unified interpretation of MCD spectra taking into account both impurity-band and valence-band contributions. Different from Ando *et al.*, they concluded that the broad positive feature was due to valence-band-to-conduction-band transitions while the negative MCD near 1.4 eV, which occurred only when the sample was fully magnetized, was due to impurity-band-related transitions.

Here we report results of a systematic MOKE spectroscopy study of $\text{Ga}_{1-x}\text{Mn}_x\text{As}$ samples with different Mn densities with three continuously varying experimental parameters: temperature (10–75 K), magnetic field (-400 to $+400$ G), and photon energy (1.4–3.1 eV). Figure 1 displays representative Kerr rotation data measured for a $\text{Ga}_{0.976}\text{Mn}_{0.024}\text{As}$ sample

(S-3) at 10 K when the magnetic field was swept between positive 400 G and negative 400 G. Strong variations of the Kerr angle are seen as a function of wavelength and magnetic field. Magnetic hysteresis is also evident by comparing the down-sweep [in Fig. 1(a)] and up-sweep [in Fig. 1(b)] data.

We focus on the *remanent* Kerr angle (i.e., the Kerr angle at zero external magnetic field), which was found to strongly depend on the photon energy, exhibiting positive peaks near 1.7 and 3 eV and a negative peak near 2.5 eV. Without an external magnetic field, the MOKE spectra were caused by the interband transitions between the spontaneously spin-split bands. The ~ 1.7 -eV peak increased in intensity and blueshifted with the Mn density and further blueshifted with annealing. Using a 30-band $\mathbf{k} \cdot \mathbf{p}$ model with antiferromagnetic sign of p - d exchange interaction, disorder broadening, and density-dependent band gap, we calculated the dielectric tensor of $\text{Ga}_{1-x}\text{Mn}_x\text{As}$ in the interband transition region and successfully reproduced the observed spectra assuming that our samples are in the metallic regime and the Mn impurity band has merged with the valence band. There was no need to add any background dielectric constant or the optical transitions involving dispersionless states located in the band gap or the conduction band in order to explain our spectra.

II. EXPERIMENTAL METHODS

The three $\text{Ga}_{1-x}\text{Mn}_x\text{As}$ samples studied were grown by low-temperature molecular beam epitaxy (LT-MBE). They have a similar structure consisting of a 50-nm epilayer of $\text{Ga}_{1-x}\text{Mn}_x\text{As}$ and a buffer layer of 1000-nm $\text{In}_{0.14}\text{Ga}_{0.86}\text{As}$ on a GaAs (001) substrate. The sample structure is depicted in the inset of Fig. 2. Sample S-1 had a nominal Mn content (x) of 0.01 and $T_c = 30$ K. Sample S-2 had a nominal Mn content of 0.024 and $T_c = 45$ K. The third sample, S-3, was from the same wafer as S-2, but it was further annealed in air at 190°C for 4 h. Its T_c was increased to 70 K. Annealing is known to remove the interstitial Mn defects (Mn_i) in LT-MBE $\text{Ga}_{1-x}\text{Mn}_x\text{As}$ and to increase the effective Mn content x and the hole density p .^{26–28} As a donor, Mn_i compensates acceptors and decreases the hole carrier concentration in the sample. Mn_i also prefers to be antiferromagnetically coupled to substitutional Mn_{sub} in such a way that it reduces the local spins in the lattice. Thus, we expect that sample S-3 has a higher concentration of holes as well as higher effective Mn_{eff} than S-2. The sample parameters are summarized in Table I. All the samples exhibited an “out-of-plane” easy axis; i.e., the magnetization direction was perpendicular to the sample surface. However, further structural and compositional information obtained via x-ray diffraction and secondary ion mass spectrometry to quantitatively determine the orientation and strength of strain in the magnetic layer is not available for these samples. Temperature-dependent magnetization of sample S-2 measured with a small perpendicular field of 50 Oe is shown in Fig. 2. A T_c of 45 K is clearly observed.

MOKE measurements were performed in the polar geometry in which the light beam was quasnormally incident on the sample surface. Figure 3(a) is a schematic diagram of the experimental setup. White light from a 100-W Xe lamp is first focused into a monochromator. Light with selected wavelength is then polarized with a Glan-Thompson polarizer

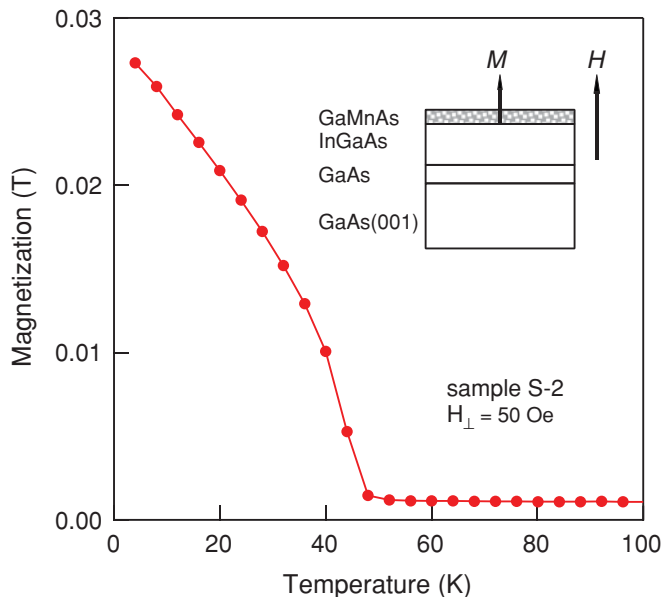


FIG. 2. (Color online) Temperature dependence of magnetization for sample S-2. A small magnetic field of 50 Oe was applied perpendicular to the sample surface. $T_c = 45$ K is revealed. Inset: sample structure.

and modulated with a mechanical chopper. The linearly polarized light impinges on the magnetic sample at a nearly normal incident angle. The reflected beam passes through a photoelastic modulator (PEM) and an analyzer, and then its intensity is detected with a Si photodiode. The current signal is amplified and converted into a voltage and fed into lock-in amplifiers. The Kerr angle caused by the different reflection of σ^\pm is proportional to the signal at the second harmonic of the PEM modulation frequency. The two lock-in amplifiers are used to demodulate the signal. The first lock-in amplifier is referenced to the chopper frequency to provide a measurement of the average light intensity at each wavelength. The second lock-in amplifier is referenced to the second harmonic of the PEM frequency to record the fast oscillating signal at 100 kHz. The Kerr rotation angle (θ_K) is derived from the ratio of these two.

Figure 3(b) schematically shows our configuration in more detail. Note that the magnetic field vector is opposite to the wave vector of the incident light. This is important in determining how the refractive indices of circularly polarized normal waves in the material are related to the components of the dielectric tensor. The Kerr angle is defined as an arctangent of the negative ratio of the y component to the x component of the reflected electric field, assuming that the incident wave propagating in the positive z direction is linearly polarized

TABLE I. $\text{Ga}_{1-x}\text{Mn}_x\text{As}$ samples studied in this paper. S-3 is annealed and the other two are not.

Sample	x	T_c (K)
S-1	0.01	30
S-2	0.024	45
S-3	0.024	70

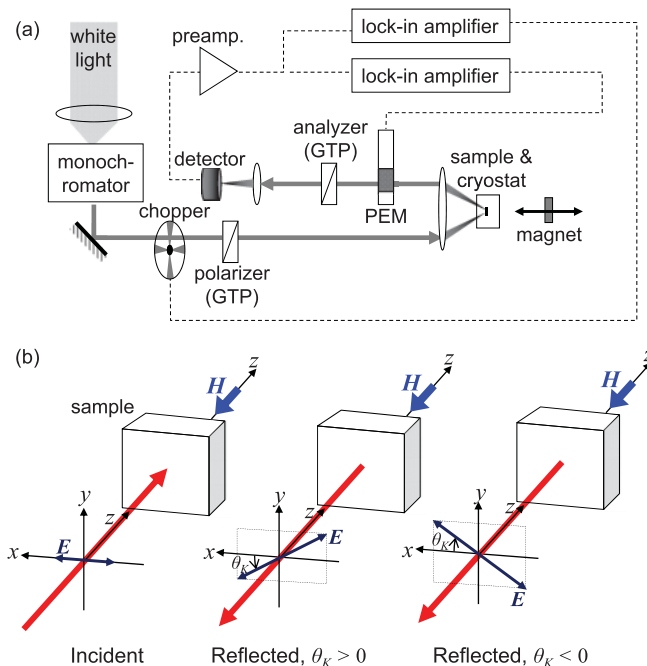


FIG. 3. (Color online) (a) Schematic diagram of the experimental setup. Light with a selected wavelength is linearly polarized, and quasnormal incident onto the sample. The reflected beam from the sample passes through a photoelastic modulator (PEM) and an analyzer, and it is detected by a photodiode. The signal is amplified and demodulated by two lock-in amplifiers. The sample is mounted inside a cryostat. Magnetic field is swept within ± 400 G. (b) Schematic diagrams showing the directions of light propagation, magnetic field, and Kerr rotation. The incident beam propagates in the positive z direction and is linearly polarized in the x direction. The reflected beam travels in the negative z direction. It becomes elliptically polarized and acquires a Kerr rotation θ_K away from the x direction as shown in the middle and right-hand panels. θ_K is defined to be positive (negative) if the rotation is clockwise (counterclockwise) when looking in the positive z direction.

in the x direction. To determine the sign of rotation, we first replace the sample with a silver mirror and induce a rotation of polarization by rotating the polarizer in front of the cryostat. Depending on the direction of rotation (clockwise or counterclockwise), there is a π phase shift in the lock-in reading. We define it to be positive if the rotation is clockwise. When the sample is mounted and a magnetic field is applied in the negative z direction, the polarization rotation (i.e., the Kerr angle) is then measured and recorded.

Samples are kept in a helium-flow cryostat, allowing us to vary the temperature (T) from 10 K to above T_c . An external magnetic field (H) is applied perpendicular to the sample surface. The coercivity and saturation field are known to be small for all three samples from superconducting quantum interference device (SQUID) measurements. Thus, the magnetic field is swept within the range between ± 400 G. The Faraday rotation induced by the cryostat window was subtracted. Any polarization anisotropy caused by components in the setup was carefully calibrated and subtracted to get the accurate Kerr rotation.

III. EXPERIMENTAL RESULTS

Hysteresis loops measured with 720 nm (1.72 eV) for samples S-2 and S-3 are compared in Fig. 4(a) at three temperatures, 10, 30, and 43 K. Generally, the annealed sample, S-3, has a larger hysteresis loop than S-2, with both larger saturation Kerr angle and increased coercive field H_c . At low temperature (10 K), the difference between the two is relatively small; the remanent Kerr angles are 0.4° and 0.38° , respectively, and the coercive fields are ~ 170 and ~ 130 G, respectively. With increasing temperature, the difference becomes more and more pronounced. The Kerr angle for sample S-2 shows sharp vertical switching near the coercive field with strong perpendicular magnetization. Annealed sample S-3 also presents strong anisotropy out of plane although the change over H_c occurs at a slightly slower rate when compared to S-2. Figures 4(b) and 4(c) display the temperature dependence of remanent θ_K (at 1.72 eV) and H_c , respectively, for S-2 and S-3. It is clearly seen that T_c increases as a result of annealing.

The photon-energy-dependent hysteresis loops, θ_K versus H , for sample S-2 are presented in Fig. 5. For each photon energy, three hysteresis loops measured below T_c ($T = 10, 30,$ and 41 K) are displayed, and the size of the loop is seen to shrink with increasing temperature. At each temperature, the vertical size of the hysteresis loop (i.e., the remanent θ_K) shows considerable variation with photon energy, while its horizontal width (i.e., the coercivity H_c) remains constant. As we can see, the hysteresis loops are sharp and well defined at most photon energies but disappear at 2.30 and 2.70 eV, although the temperature is below T_c . In addition, the sign of remanent θ_K depends on the photon energy. With the same

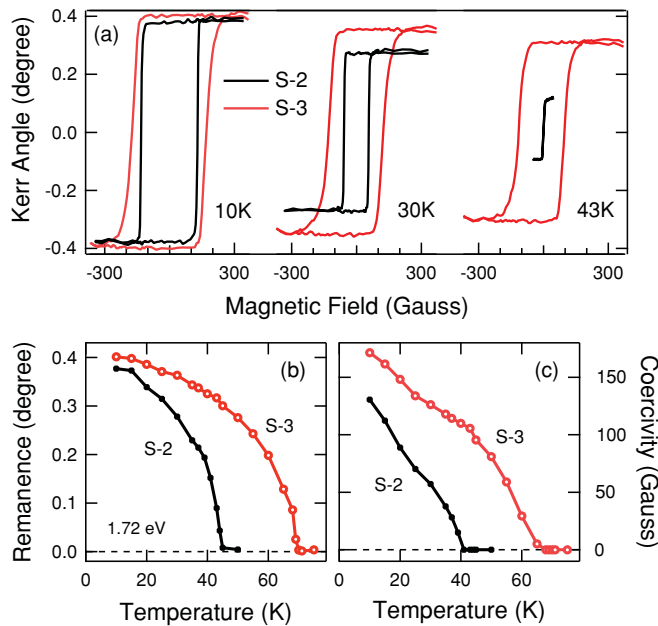


FIG. 4. (Color online) (a) Hysteresis loops (720 nm) detected for samples S-2 and S-3 at 10, 30, and 43 K. Annealed sample S-3 exhibits a larger saturation Kerr angle and coercive field at all temperatures. Temperature dependence of the (b) remanent Kerr angle and (c) coercivity for S-2 and S-3.

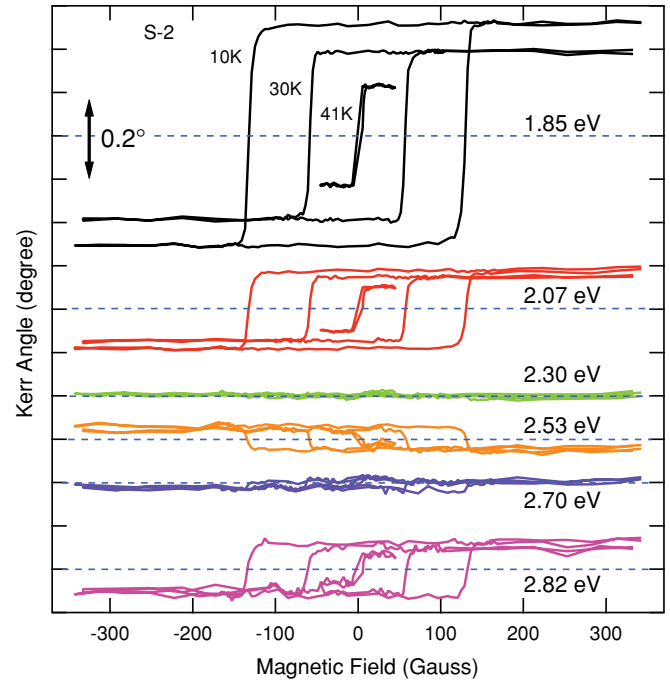


FIG. 5. (Color online) Temperature-dependent hysteresis loops detected with different photon energies for sample S-2. Both the magnitude and the sign of the remanent Kerr angle change with photon energy. For clarity, the hysteresis loops are vertically offset.

sweeping direction, the hysteresis loop at 2.53 eV varies in the opposite way of that at 2.07 and 2.82 eV.

Remanent Kerr spectra (θ_K at $H = 0$ versus photon energy) for sample S-3 at various T (from 10 to 75 K) are shown in Fig. 6(a). Above T_c , there is no Kerr signal left. Below T_c , each spectrum contains a pronounced positive peak at ~ 1.72 eV and a weaker positive peak at ~ 3 eV. The spectrum flips signs in the range 2.4–2.7 eV. With increasing temperature, the main 1.72-eV peak remains in the same spectral position, while the magnitude decreases and finally disappears above 70 K. Spectra for S-1 and S-2 were essentially the same as that for S-3, except that the main peaks occurred at slightly lower energies. Spectra for all three samples at 20 K are plotted together in Fig. 6(b). We clearly see that the main peak shifts from 1.65 eV in S-1 to 1.7 eV in S-2 and to 1.72 eV in S-3, due to increasing Mn content (S-1 to S-2 and S-2 to S-3) and annealing (S-2 to S-3).

IV. THEORETICAL MODELING

A. Band structure calculation

Our theoretical model is based on the $\mathbf{k} \cdot \mathbf{p}$ method^{29–32} and treats the antiferromagnetic exchange coupling between the hole spins in the host semiconductor and the substitutional Mn^{2+} spins within the mean-field approximation.^{33–37} Recently, this approach was used to explain observed MO effects in $\text{Ga}_{1-x}\text{Mn}_x\text{As}$ in the metallic regime, especially in the infrared spectral region near the Fermi level located inside the valence band.²² Here we model our experimental magneto-optical Kerr spectra in the interband region with a similar approach, but using a full band structure obtained with

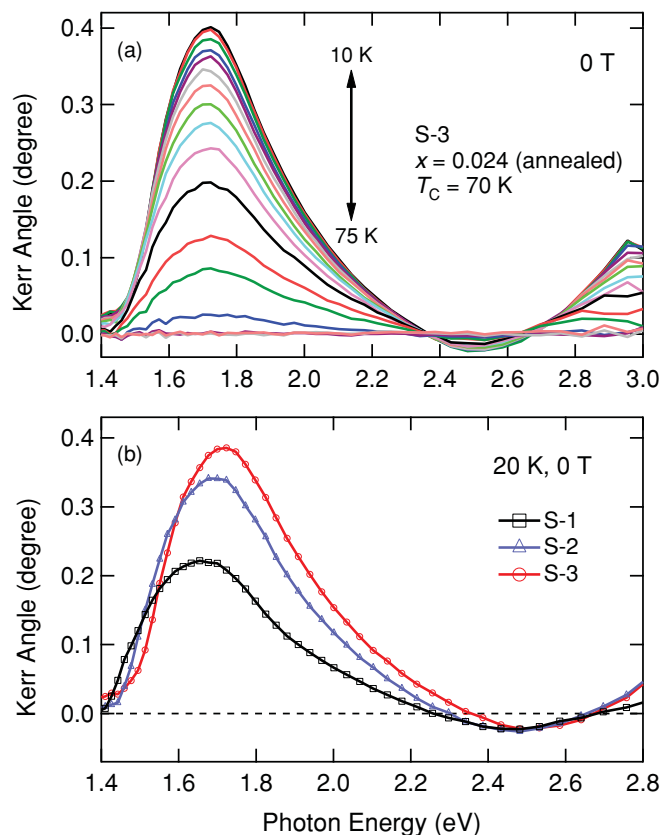


FIG. 6. (Color online) (a) Remanent ($H = 0$) Kerr spectra at different temperatures for S-3. (b) Remanent Kerr spectra at 20 K for S-1, S-2, and S-3. The main peak at 1.7 eV shifts to higher energy with increasing Mn content (from S-1 to S-2) and annealing (from S-2 to S-3).

a 30-band $\mathbf{k} \cdot \mathbf{p}$ method³¹ instead of the effective band structure calculation based on the two-level model, which includes only Γ_{6C} and Γ_{8V}/Γ_{7V} (here we follow the T_d double group notation throughout the paper). We show that this approach provides qualitatively reasonable results in reproducing the measured Kerr spectra and magnetization.

To model MOKE spectra up to ~ 3 eV, the extension to the full band structure is critical, since the 8-band $\mathbf{k} \cdot \mathbf{p}$ method based on the two-level model, which is often employed to explain the electronic band structure of metallic $\text{Ga}_{1-x}\text{Mn}_x\text{As}$, is valid only up to $k \sim 0.1 \text{ \AA}^{-1}$ measured from the Γ edge, in both the conduction band and the valence band. Optical transitions with energy ~ 3 eV involve states with k -vectors higher than the above value, where the two-level model breaks down. Furthermore, the dielectric tensor in the spectral range of interest obtains significant contributions from transitions with energies higher than 3 eV. Simulations based on the 8-band $\mathbf{k} \cdot \mathbf{p}$ model have to include an adjustable static dielectric constant added by hand.

Furthermore, within the two-level $\mathbf{k} \cdot \mathbf{p}$ model, one needs to specify the Luttinger parameters to take into account the interaction of the valence band with remote bands. The 30-band Hamiltonian does not contain the Luttinger parameters; instead, the coupling between bands is described in terms of the matrix elements and band edges that are retrieved from the experiments. Once the band structure is

determined with the 30-band method, one can calculate the Luttinger parameters^{31,32} for the subsequent use in simplified 8-band calculations. This is an important advantage of the 30-band $\mathbf{k} \cdot \mathbf{p}$ method as compared to the 8-band $\mathbf{k} \cdot \mathbf{p}$ method. Therefore, the modification of the valence-band interaction with remote bands due to antiferromagnetic Mn-hole spin exchange coupling, strain, and Coulomb interaction effects in diluted magnetic semiconductors can be simultaneously taken into account within the 30-band $\mathbf{k} \cdot \mathbf{p}$ model. Also, the lack of inversion symmetry is taken into account through the matrix element between Γ_{6C} and Γ_{8V}/Γ_{7V} .

The extended $\mathbf{k} \cdot \mathbf{p}$ method is known to be valid up to 5 eV above and 6 eV below the top of the valence band, covering interband transitions of energies up to 11 eV. It has been successfully applied to calculate effective masses and g factors for the group IV and III-V semiconductors.^{31,38} The general shortcomings of the method are also known, e.g., limited experimental data for higher conduction bands, and the numerical difficulty in ensuring the continuity between U and K symmetry points. The accuracy of the GaAs band structure calculations with the 30-band method is discussed, e.g., in Ref. 31. Here we do not reproduce all the complicated basis orbitals, energy-level structures, band-edge energies, and matrix elements for pure GaAs in a 30-band model; instead we refer the reader to Refs. 31 and 32.

Our model Hamiltonian matrix is expressed as

$$H_T^{ij} = H_0^{ij} + H_{\text{strain}}^{ij} + H_{\text{spin-ex}}^{ij}, \quad (1)$$

$$H_{\text{strain}}^{ij} = \sum_{\alpha, \beta} \langle i | D^{\alpha\beta} | j \rangle \varepsilon_{\alpha\beta}^{\text{strain}},$$

$$H_{\text{spin-ex}}^{ij} = \sum_I^{N_{\text{Mn}}} \langle i | J(\mathbf{r} - \mathbf{R}_I) \mathbf{S}_I \cdot \mathbf{s}_{\text{sc}} | j \rangle$$

$$\approx J_{ij} N_{\text{Mn}} S_{\text{Mn}} \langle i | \hat{\mathbf{s}}_{\text{sc}} | j \rangle,$$

where

$$\langle i | D^{\alpha\beta} | j \rangle = -\frac{(p_\alpha p_\beta)_{ij}}{m} + V_{ij}^{\alpha\beta}. \quad (2)$$

In the preceding equations, H_0^{ij} is a 30-band $\mathbf{k} \cdot \mathbf{p}$ matrix, H_{strain}^{ij} is the strain Hamiltonian matrix, and $\varepsilon_{\alpha\beta}^{\text{strain}}$ is the strain tensor, in which all off-diagonal elements are zero; α and β are coordinates; $\langle i | D^{\alpha\beta} | j \rangle$ consists of the linear combination of the deformation potentials³⁰; m is the bare electron mass; and $H_{\text{spin-ex}}^{ij}$ describes the spin-exchange interaction between the substitutional Mn magnetic impurity spins and the itinerant charge carrier spins in the host semiconductor within the mean-field approximation. The indices i and j run over all 30-band basis orbitals. The antiferromagnetic spin-exchange constant J_{ij} is nonzero only when the bases correspond to Γ_{6C} , Γ_{8V} , and Γ_{7V} ; $J_{ij} = 54 \text{ meV nm}^3$ for Γ_{8V}/Γ_{7V} , $J_{ij} = -9 \text{ meV nm}^3$ for Γ_{6C} ,^{39,40} and $N_{\text{Mn}} = 4/a_{\text{Ga}_{1-x}\text{Mn}_x\text{As}}^3$, where $a_{\text{Ga}_{1-x}\text{Mn}_x\text{As}}$ is the lattice constant of $\text{Ga}_{1-x}\text{Mn}_x\text{As}$. The strain effects are included only for the bases Γ_{6C} , Γ_{8V} , and Γ_{7V} . In this approximation, the Γ edges of Γ_{6C} , Γ_{8V} , and Γ_{7V} states are shifted by strain in the same way as those in the 8-band model.

We qualitatively took into account many-body Coulomb interactions through the phenomenological bandgap narrowing

(BGN). The hole-occupied exchange spin-split Γ_{8V} bands were assumed to be rigidly shifted by an amount $ap^{1/3}$, where $a = 2.6 \times 10^{-8}$ cm eV and p is in cm^{-3} .⁴¹ The proportionality constant is compatible with that used in Ref. 22. Several iterations were necessary to obtain self-consistent positions of the Γ_{8V} edges and the Fermi level. Still, the resulting BGN shifts are only qualitative; rigorous calculations will be attempted elsewhere. The disorder effect was also phenomenologically described as broadening of interband optical transitions (~ 100 meV half width at half maximum) in the linear dielectric response function.

The thermal fluctuations of Mn spin ordering at temperature $T = 20$ K, at which the experimental data in Fig. 6(b) were obtained, can be roughly estimated by comparing the measured amplitudes of the remanent Kerr angle as a function of an external magnetic field at 10 and 20 K. The effect of thermal fluctuations was included in the calculation of temperature-dependent dielectric tensors and Kerr-angle spectra. The temperature dependence of other physical parameters, for example, the band gap, the lattice constant, the strain tensor, and the hole density, were assumed to be negligible in this narrow temperature range.

We assumed that our samples only had the epitaxial biaxial tensile strain (see Sec. II), which breaks the crystallographic cubic symmetry due to the lattice mismatch between the $\text{Ga}_{1-x}\text{Mn}_x\text{As}$ epilayer and the relaxed GaInAs buffer layer. The same strain parameters as for GaAs (Ref. 42) were used for the $\text{Ga}_{1-x}\text{Mn}_x\text{As}$ epilayer except for its lattice constant. Depending on the Mn (2%~5%) and In (9.5%) contents, the strain tensor $\varepsilon_{ii}^{\text{strain}}$ ($i = x, y, z$) varies from 0.4% to 0.57% for the MnAs lattice constant 5.98 Å.⁵ We assumed that our experimental postgrowth procedure did not produce any additional significant strain. An example of the band structure calculated with the 30-band $\mathbf{k} \cdot \mathbf{p}$ method for 5% Mn is shown in Fig. 7.

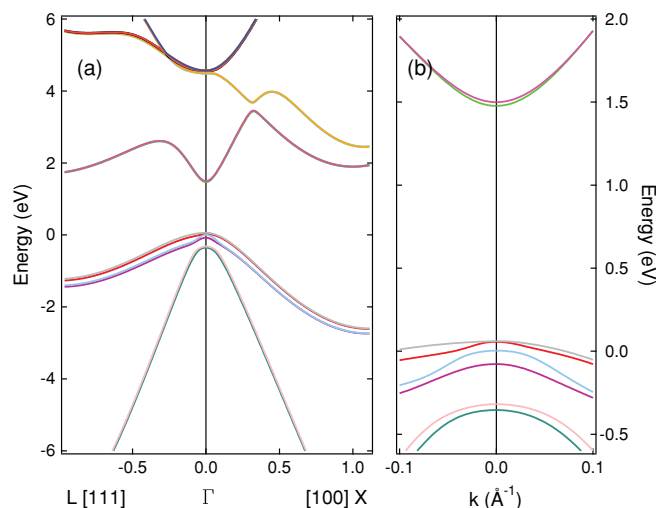


FIG. 7. (Color online) Band structure of $\text{Ga}_{0.95}\text{Mn}_{0.05}\text{As}$, calculated through the 30-band $\mathbf{k} \cdot \mathbf{p}$ method described in the text, taking into account the Mn-hole spin-exchange interaction as well as a biaxial tensile strain of $\varepsilon_{xx}^{\text{strain}} = +0.4\%$. The right-hand panel shows a magnified band structure near $k = 0$.

B. Hole densities and magnetic anisotropy

Before proceeding with the calculation of the frequency-dependent dielectric tensor and magneto-optical Kerr-angle spectra, we roughly estimate the hole densities and Curie temperatures in our samples by calculating temperature-dependent magnetization based on the mean-field Zener model.^{35,36} In addition, we determine the easy axis of magnetization with the estimated hole densities obtained for various Mn fractions. These provide not only guidelines for the subsequent Kerr-angle calculation but also justification for the results obtained by the extended $\mathbf{k} \cdot \mathbf{p}$ method in the metallic regime in the interband range. To calculate the ferromagnetic critical temperature, temperature-dependent magnetization, and magnetic anisotropy, we use the 8-band $\mathbf{k} \cdot \mathbf{p}$ method since these quantities depend only on the very top portion of the valence band structure.

The temperature-dependent magnetization in Fig. 8 was calculated in the limit of strong degeneracy with zero external magnetic field based on the mean-field Zener model.³⁶ Table II lists the hole densities for various nominal Mn fractions, for which the calculated Curie temperatures are equal to the experimental ferromagnetic phase transition temperatures obtained from the SQUID measurement of the temperature-dependent magnetization in sample S-2 (Fig. 2) and the measurement of the saturated remanent Kerr angle as a function of temperature (Fig. 4). The calculation neglects the Fermi-liquid effect, which increases T_c ,³⁶ as well as the spin-wave excitations,³⁷ which decrease T_c for a given Mn fraction and a hole density. We simulate the annealing effect,²⁷ which increased T_c to 70 K for sample S-3, by increasing the hole density for each Mn fraction. Note that generally not

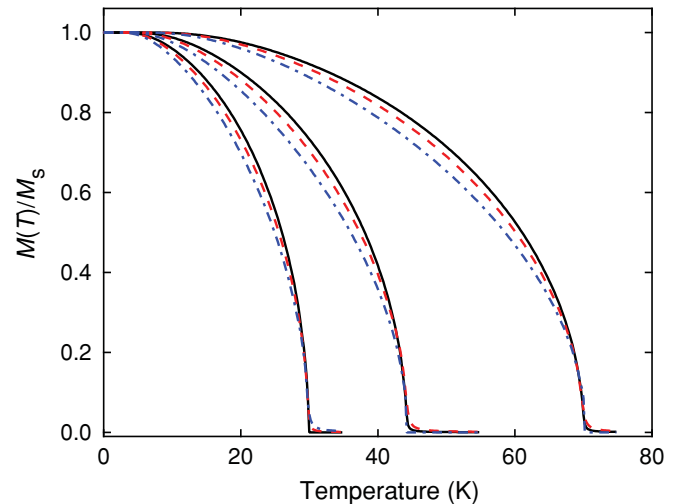


FIG. 8. (Color online) Calculated temperature-dependent normalized magnetization based on the mean-field Zener model and the 8-band $\mathbf{k} \cdot \mathbf{p}$ method with different Mn fractions $x = 0.03$ [solid (black) lines], 0.04 [dashed (red) lines], and 0.05 [dash-dotted (blue) lines] for $T_c = 45$ K (sample S-2) and 70 K (annealed sample, S-3), and with $x = 0.02$ [solid (black) lines], 0.03 [dashed (red) lines], and 0.04 [dash-dotted (blue) lines] for $T_c = 30$ K (sample S-1). The corresponding hole densities for each case are summarized in Table II. The results are all for the tensile strain $\varepsilon_{xx}^{\text{strain}} = (0.57, 0.52, 0.46, 0.4)\%$ for Mn fraction $x = (0.02, 0.03, 0.04, 0.05)$.

TABLE II. Hole densities calculated for various Mn fractions based on the 8-band $\mathbf{k} \cdot \mathbf{p}$ method and the mean-field Zener model for the measured Curie temperatures of our samples.

$T_c(K)$	Mn (%)	Hole density, p (10^{20} cm^{-3})
45 (S-2)	3	2.35
	4	1.6
	5	1.2
70 (S-3)	3	5
	4	3.05
	5	2.2
30 (S-1)	2	2.4
	3	1.39
	4	0.97

only does the hole density increase, but the lattice constant of $\text{Ga}_{1-x}\text{Mn}_x\text{As}$ is also reduced upon annealing.²⁸

The magnetocrystalline anisotropy, caused by the spin-orbit interaction, is attributed to the valence band holes since the total angular momentum of the local Mn moments is solely due to spins. The anisotropy gives certain preferred directions for the spins to be aligned in crystals, so the easy direction of magnetization is determined. We estimated the anisotropy field, which is proportional to the difference of hole free energies in [001] and [100] directions,³⁶ for different nominal Mn fractions, showing magnetic easy axes under tensile strain as a function of hole density as shown in Fig. 9. All hole densities shown in Table II fall into the out-of-plane magnetic easy axis case ([001]) because they are all larger than the critical hole density for each Mn fraction, in which the easy axis is changed from [100] to [001]. The out-of-plane easy axis is further confirmed by the single-domain-like behavior

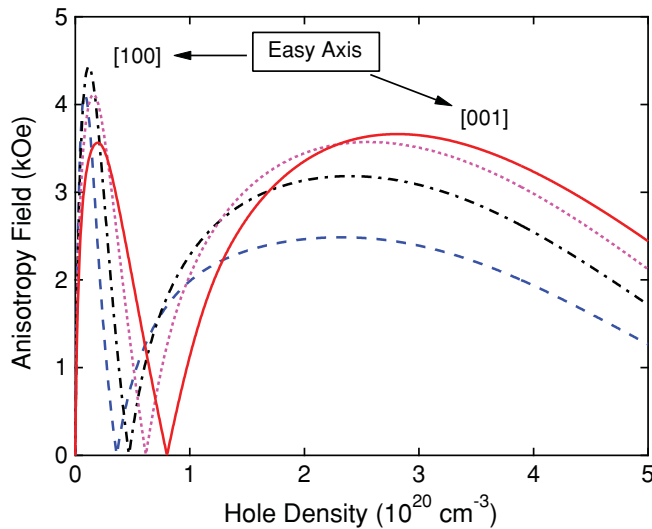


FIG. 9. (Color online) Anisotropy field, H_{an} , calculated with the 8-band $\mathbf{k} \cdot \mathbf{p}$ model, as a function of hole density under tensile strain $\epsilon_{xx}^{\text{strain}} = (0.57, 0.52, 0.46, 0.4)\%$ for Mn fractions $x = (0.02, 0.03, 0.04, 0.05)$, respectively. The magnetic easy axes of our samples are out of plane ([001]) for the hole densities shown in Table II. The curves are for Mn fractions $x = 0.02$ (dashed line), 0.03 (dash-dotted line), 0.04 (dotted line), and 0.05 (solid line).

TABLE III. Chosen Mn fractions and corresponding hole densities for $T_c = 45$ K (sample S-2), $T_c = 30$ K (S-1), and $T_c = 70$ K (S-3) used in the dielectric function and Kerr-angle calculations by the 30-band $\mathbf{k} \cdot \mathbf{p}$ method. The resulting Kerr-angle spectra are shown in Figs. 11, 12, and 13, respectively.

$T_c(K)$	Mn (%)	Hole density, p (10^{20} cm^{-3})	
45	3	2	
	3	2.5	
	3	3	
	4	1	
	4	1.5	
	4	2	
	5	1	
	5	1.5	
	30	2	2
		2	2.5
		2	3
		3	1.2
		3	1.4
		3	1.6
		4	0.8
4		1	
4		1.2	
70	4	2.5	
	4	3	
	4	3.5	
	5	2	
	5	2.5	

in the hysteresis loops of the measured remanent Kerr angles for the applied out-of-plane external magnetic field shown in Fig. 4.

C. Frequency-dependent dielectric tensor and Kerr angle spectra

With the estimated hole densities and magnetic easy axis directions, calculations of the dielectric tensor were performed based on the linear response theory (or the Kubo formula^{43–45}) shown in Eq. (3) for several different hole densities (shown in Table III from the range of the hole densities and Mn fractions calculated for our samples in the previous section; see Table II):

$$\begin{aligned} \epsilon_{\alpha\beta}(\omega) = & \delta_{\alpha\beta} + \frac{e^2 \hbar^2}{m_0^2 \epsilon_0} \frac{1}{(2\pi)^3} \sum_{\substack{a,b \\ a \neq b}} \int \int \int_{\text{BZ}} f_a \frac{1}{(E_{ba})^2} \\ & \times \left[\frac{P_{ab}^\alpha P_{ba}^\beta}{(E_{ba} - i\hbar\gamma - \hbar\omega)} + \frac{P_{ba}^\alpha P_{ab}^\beta}{(E_{ba} + i\hbar\gamma + \hbar\omega)} \right] \\ & \times dk_x dk_y dk_z, \end{aligned} \quad (3)$$

where α and β denote coordinates and a and b represent valence bands and conduction bands, respectively. Only interband transitions are included in calculations; f_a is the Fermi-Dirac distribution and p_{ab}^α are components of the momentum matrix element. The integration is extended over the first Brillouin zone using full band structure calculated with

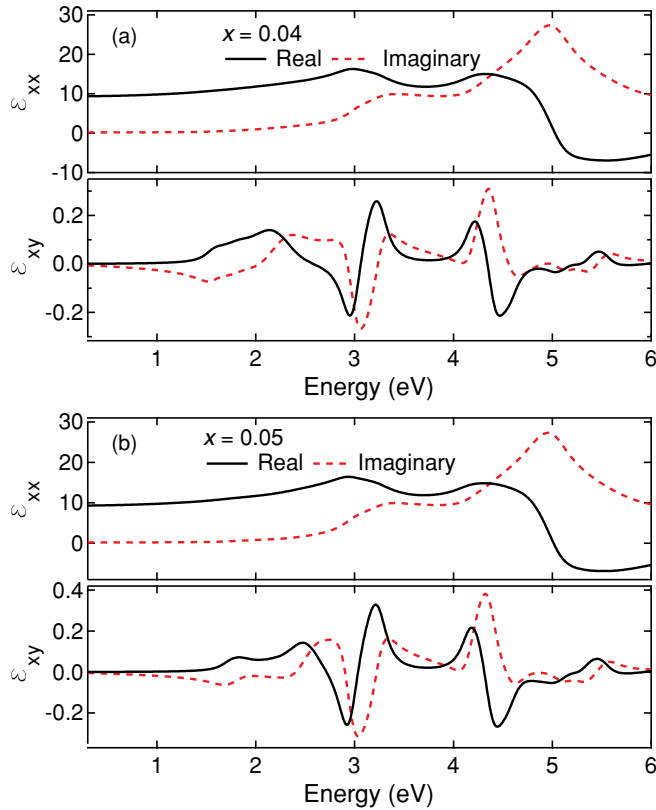


FIG. 10. (Color online) Complex dielectric functions ϵ_{xx} and ϵ_{xy} for 4% Mn, $p = 1 \times 10^{20} \text{ cm}^{-3}$, and 5% Mn, $p = 1.5 \times 10^{20} \text{ cm}^{-3}$, under tensile biaxial strain.

the 30-band $\mathbf{k} \cdot \mathbf{p}$ method described in Sec. IV A. An example of the calculated dielectric tensor is shown in Fig. 10.

Note that the above approach is based on matrix elements determined for a clean GaAs material. An important and still open question is whether and how one can modify the $\mathbf{k} \cdot \mathbf{p}$ matrix elements in a meaningful way to provide a more adequate description of heavily disordered systems. One approach to calculating the optical f -sum rule and its associated optical mass in disordered systems in the infrared range was presented in Ref. 46. However, the matrix elements and the Luttinger parameters in the band structure in this reference are still based on the clean GaAs. Moreover, the 18 matrix elements cannot be adjusted simultaneously by simply fitting optical masses in a disordered system. Other methods of band structure calculations may be needed, and any modeling has to be supplemented with extensive systematic studies of materials with varying degrees of disorder to establish empirical values providing the best fit.

Once frequency-dependent dielectric functions are obtained, calculating Kerr-angle spectra is straightforward, taking into account all effects of propagation and reflections in a thin $\text{Ga}_{1-x}\text{Mn}_x\text{As}$ layer and the buffer layer. For the dielectric function of the GaInAs buffer layer, the linear interpolation of the experimental data⁴⁷ for GaAs and InAs was used. The calculated Kerr-angle results are shown in Fig. 11 for sample S-2. Note that, for a fixed Mn fraction, the Kerr-angle peak magnitude decreases with increasing hole density. This happens because at these densities the Fermi level is already

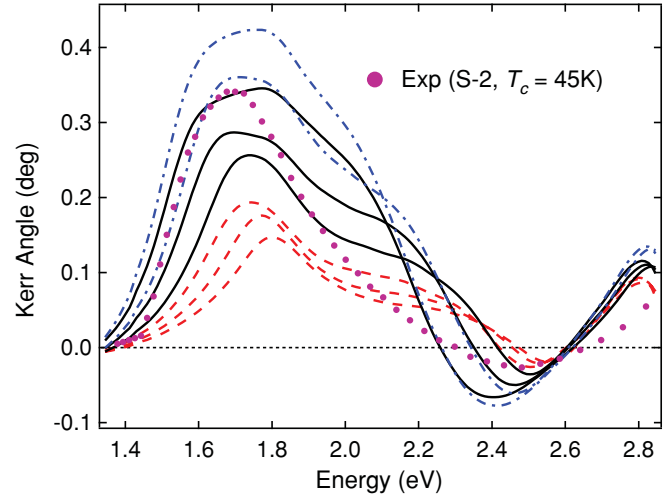


FIG. 11. (Color online) Calculated frequency-dependent magneto-optical Kerr angle under tensile strain by the 30-band $\mathbf{k} \cdot \mathbf{p}$ method in the interband transition range for various hole densities and three different Mn fractions $x_{\text{Mn}} = 0.03$ [dashed (red) lines], 0.04 [solid (black) lines], and 0.05 [dash-dotted (blue) lines] with $\text{Ga}_{1-x}\text{Mn}_x\text{As}$ epilayer thickness 70 nm. Hole densities (see Table III) were chosen with the range of $\sim \pm 5 \times 10^{19} \text{ cm}^{-3}$ around the hole density corresponding to $T_c = 45 \text{ K}$ (sample S-2). For each Mn fraction, the higher peak corresponds to a lower hole density.

located below the lowest band edge of the spin-split Γ_{8V} . With increasing hole density, the Fermi level is shifted further downward, which reduces the number of states that contribute to interband optical transitions. On the other hand, if the Fermi level were initially in the middle of the spin-split Γ_{8V} , increasing the hole density would not necessarily decrease the Kerr-angle amplitude.

Kerr-angle calculation results for 4% Mn give the best agreement with the experimental MOKE spectra of S-2, as shown in Fig. 11. The first positive peak that can be attributed to the interband transitions around the E_0 critical point is redshifted due to phenomenological bandgap narrowing of 0.121 and 0.138 eV, respectively, for each case. Note that the above Mn fractions are 1.5 to 2 times larger than the experimental nominal value, 2.4% for S-2, as we discuss in Sec. V.

For sample S-1, the calculated result for Kerr angles is closest to the experimental MOKE spectra for 3% Mn, as shown in Fig. 12 and Table III. This Mn fraction is also larger than the experimental value of 1.5% for sample S-1.

In Table II, the hole densities that are predicted for $T_c = 70 \text{ K}$ based on the 8-band $\mathbf{k} \cdot \mathbf{p}$ model are overestimated since at large hole densities the hole free energy calculated with the 8-band $\mathbf{k} \cdot \mathbf{p}$ model becomes noticeably smaller than that calculated with the full-band model. This originates from the difference between the valence band structures calculated with these two models at large k . Therefore, it is expected that the full band structure calculation yields hole densities smaller than those listed in Table II. Note also that with 4% or 5% Mn fraction, the Kerr-angle calculation agrees better with the experimental Kerr spectra for $T_c = 45 \text{ K}$ (S-2), as shown in Fig. 11. Therefore, for the annealed case of $T_c = 70 \text{ K}$, the

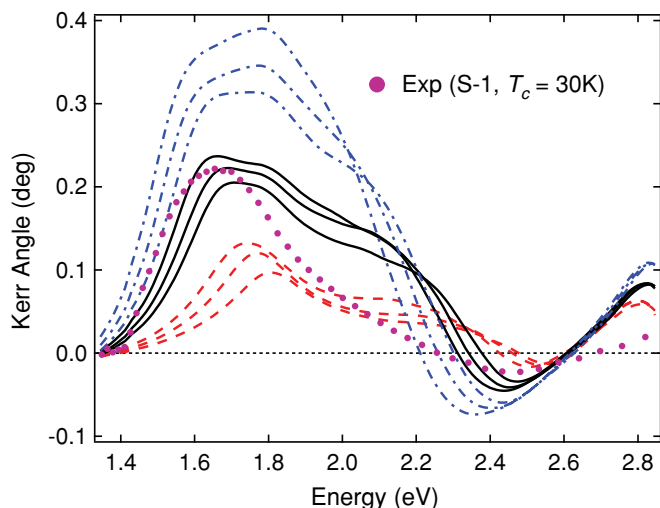


FIG. 12. (Color online) Frequency-dependent magneto-optical Kerr angle under tensile strain calculated through by the 30-band $\mathbf{k} \cdot \mathbf{p}$ method in the interband transition range for various hole densities and three different Mn fractions $x_{\text{Mn}} = 0.02$ [dashed (red) lines], 0.03 [solid (black) lines], and 0.04 [dash-dotted (blue) lines] with $\text{Ga}_{1-x}\text{Mn}_x\text{As}$ epilayer thickness of 70 nm . Hole densities (Table III) were chosen around the estimated hole densities at $T_c = 30\text{ K}$ from Table II (sample S-1). For each Mn fraction, corresponding hole densities are smaller from the top.

Kerr-angle calculations are performed only for 4% and 5% Mn fractions. The results are shown in Fig. 13, and their corresponding hole densities are listed in Table III.

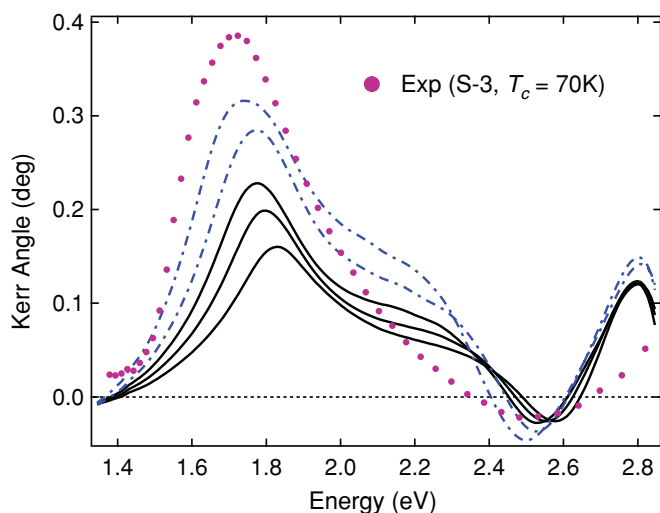


FIG. 13. (Color online) Frequency-dependent magneto-optical Kerr angle calculated through the 30-band $\mathbf{k} \cdot \mathbf{p}$ method in the interband transition range for various hole densities and two different Mn fractions $x_{\text{Mn}} = 0.04$ [solid (black) lines] and 0.05 [dash-dotted (blue) lines] with $\text{Ga}_{1-x}\text{Mn}_x\text{As}$ epilayer thickness of 70 nm . Hole densities (shown in Table III) were chosen around the estimated hole densities (Table II) for $T_c = 70\text{ K}$ (sample S-3) obtained by the 8-band $\mathbf{k} \cdot \mathbf{p}$ method and the mean-field Zener model. For each Mn fraction, corresponding hole densities are smaller from the top.

V. DISCUSSION

Our calculated MOKE spectra of ferromagnetic $\text{Ga}_{1-x}\text{Mn}_x\text{As}$ samples in the interband transition range reveal a general pattern of a large-amplitude positive peak around $1.4\text{--}2.3\text{ eV}$ followed by negative and positive peaks with lower amplitudes at higher photon energies, similar to the experimental data. At the same time, the quantitative spectral shapes and the positions of the peaks sensitively depend on the amount of substitutional Mn, the hole density, and the layer thickness. We determined the range of Mn fractions and corresponding hole densities for which the calculated Curie temperatures were equal to the experimentally measured ferromagnetic transition temperatures. Then the parameters from this range providing the best fit to the measured MOKE spectra were found. The resulting Mn fractions turned out to be larger than the experimental nominal doping values for all samples. If we assume that the experimental Mn concentrations are quite accurate, this result could indicate that antiferromagnetic p - d exchange coupling strengths are 1.5 to 2 times stronger than the value of J_{ij} adopted in the simulations. This is because, in the mean-field approximation that we used throughout the calculations, the exchange coupling Hamiltonian contains the product of N_{Mn} and J_{ij} , as shown in Eq. (1).

Unlike magnetic circular dichroism, which has a clear physical interpretation as the difference of absorption coefficients between the σ^- and σ^+ polarizations, it is difficult to extract a single physical parameter that determines the characteristics of the Kerr-angle spectra in a thin-layer limit¹⁸ since the contribution of the $\text{Ga}_{1-x}\text{Mn}_x\text{As}$ layer thickness, diagonal and off-diagonal components of dielectric functions, and the dielectric function of the buffer layer should be explicitly considered. However, the first positive peak can still be attributed to the interband transitions around the E_0 critical point. The position of this peak and those of subsequent peaks are affected by the layer thickness. Figure 14 shows a set of calculated MOKE spectra for a fixed Mn fraction (4%) and

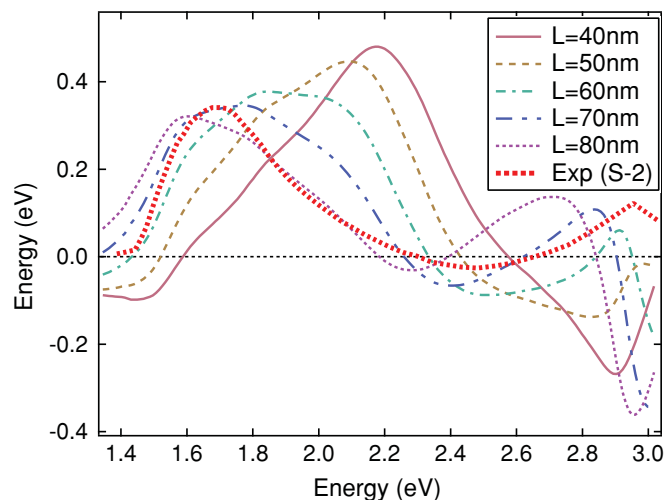


FIG. 14. (Color online) Calculated MOKE spectra for ferromagnetic $\text{Ga}_{1-x}\text{Mn}_x\text{As}$ with different layer thicknesses for 4% Mn fraction and hole density of $1 \times 10^{20}\text{ cm}^{-3}$. The dotted line shows the experimental spectrum for sample S-2.

hole density ($p = 1 \times 10^{20} \text{ cm}^{-3}$) but different thicknesses of the $\text{Ga}_{1-x}\text{Mn}_x\text{As}$ epilayer. The Kerr-angle peaks redshift as the thickness increases. The best match to the spectrum of sample S-2 is obtained when the layer thickness is about 70 nm, which is somewhat higher than our nominal value of 50 nm.

For the annealed sample (S-3), the main peak in the measured MOKE spectrum shows a slightly increased amplitude as well as a slight blueshift compared to that before annealing (S-2). If we assume that the only effect of annealing is an increased hole density for a given Mn fraction, our simulations predict an opposite trend: a decrease in the amplitude of the Kerr-angle peak with increasing hole density. Within the mean-field approximation, the observed effect of annealing indicates that the annealing also leads to an increase in the exchange interaction energy through an increase in the Mn fraction and/or J_{ij} .

VI. CONCLUSIONS

We used the magneto-optical Kerr effect to investigate three $\text{Ga}_{1-x}\text{Mn}_x\text{As}$ samples with out-of-plane magnetic easy axis anisotropy but different Mn densities. We measured the magneto-optical Kerr rotation as a function of three continuously varying parameters: photon energy, magnetic field, and temperature. We observed remanent Kerr spectral

peaks near 1.7 eV, which increased in intensity and blueshifted with Mn doping and further blueshifted with annealing. We presented theoretical modeling of magnetic and optical properties of ferromagnetic $\text{Ga}_{1-x}\text{Mn}_x\text{As}$ using the mean-field approximation and the 30-band $\mathbf{k} \cdot \mathbf{p}$ method, in which interband optical transitions are calculated over the whole first Brillouin zone and modified valence-band interactions with remote bands affected by the Mn-hole spin exchange interaction, the biaxial strain, and the phenomenological Coulomb interaction and disorder effect are explicitly and simultaneously taken into account. Our calculation of MOKE spectra of thin-film ferromagnetic $\text{Ga}_{1-x}\text{Mn}_x\text{As}$ samples in the metallic regime is in good qualitative agreement with the experimental spectra. To treat the MOKE spectra more rigorously in the interband range within the full band $\mathbf{k} \cdot \mathbf{p}$ method, the k -dependent self-energy, which explicitly takes into account many-body Coulomb interaction and disorder effects, has to be calculated.

ACKNOWLEDGMENTS

Y.-H. Cho and A. Belyanin acknowledge many helpful discussions with J. Sinova and T. Jungwirth. This work was supported by the NSF through Awards No. OISE-0530220 and No. ECS-0547019.

*kono@rice.edu

- ¹J. K. Furdyna and J. Kossut, eds., *Diluted Magnetic Semiconductors, Semiconductors and Semimetals* (Academic, Boston, 1988), Vol. 2.
- ²H. MuneKata, H. Ohno, S. von Molnár, A. Segmüller, L. L. Chang, and L. Esaki, *Phys. Rev. Lett.* **63**, 1849 (1989).
- ³H. Ohno, H. MuneKata, T. Penney, S. von Molnár, and L. L. Chang, *Phys. Rev. Lett.* **68**, 2664 (1992).
- ⁴H. MuneKata, A. Zaslavski, P. Fumagalli, and R. J. Gambino, *Appl. Phys. Lett.* **63**, 2929 (1993).
- ⁵H. Ohno, A. Shen, F. Matsukara, A. Oiwa, A. Endo, S. Katsumoto, and Y. Iye, *Appl. Phys. Lett.* **69**, 363 (1996).
- ⁶V. Novák, K. Olejník, J. Wunderlich, M. Cukr, K. Výborný, A. W. Rushforth, K. W. Edmonds, R. P. Campion, B. L. Gallagher, J. Sinova *et al.* *Phys. Rev. Lett.* **101**, 077201 (2008).
- ⁷A. H. MacDonald, P. Schiffer, and N. Samarth, *Nat. Mater.* **4**, 195 (2005).
- ⁸S. Koshihara, A. Oiwa, M. Hirasawa, S. Katsumoto, Y. Iye, C. Urano, H. Takagi, and H. MuneKata, *Phys. Rev. Lett.* **78**, 4617 (1997).
- ⁹H. Ohno, D. Chiba, F. Matsukara, T. Omiya, E. Abe, T. Dietl, Y. Ohno, and K. Ohtani, *Nature* **408**, 944 (2000).
- ¹⁰K. Ando, T. Hayashi, M. Tanaka, and A. Twardowski, *J. Appl. Phys.* **83**, 6548 (1998).
- ¹¹J. Szczytko, W. Mac, A. Twardowski, F. Matsukura, and H. Ohno, *Phys. Rev. B* **59**, 12935 (1999).
- ¹²B. Beschoten, P. A. Crowell, I. Malajovich, D. D. Awschalom, F. Matsukura, A. Shen, and H. Ohno, *Phys. Rev. Lett.* **83**, 3073 (1999).
- ¹³J. Okabayashi, A. Kimura, O. Rader, T. Mizokawa, A. Fujimori, T. Hayashi, and M. Tanaka, *Phys. Rev. B* **64**, 125304 (2001).

- ¹⁴T. Komori, T. Ishikawa, T. Kuroda, J. Yoshino, F. Minami, and S. Koshihara, *Phys. Rev. B* **67**, 115203 (2003).
- ¹⁵E. J. Singley, K. S. Burch, R. Kawakami, J. Stephens, D. D. Awschalom, and D. N. Basov, *Phys. Rev. B* **68**, 165204 (2003).
- ¹⁶K. S. Burch, J. Stephens, R. K. Kawakami, D. D. Awschalom, and D. N. Basov, *Phys. Rev. B* **70**, 205208 (2004).
- ¹⁷K. S. Burch, D. B. Shrekenhamer, E. J. Singley, J. Stephens, B. L. Sheu, R. K. Kawakami, P. Schiffer, N. Samarth, D. D. Awschalom, and D. N. Basov, *Phys. Rev. Lett.* **97**, 087208 (2006).
- ¹⁸R. Lang, A. Winter, H. Pascher, H. Krenn, X. Liu, and J. K. Furdyna, *Phys. Rev. B* **72**, 024430 (2005).
- ¹⁹R. Chakarvorty, S. Shen, K. J. Yee, T. Wojtowicz, R. Jakiela, A. Barcz, X. Liu, J. K. Furdyna, and M. Dobrowolska, *Appl. Phys. Lett.* **91**, 171118 (2007).
- ²⁰K. Ando, H. Saito, K. C. Agarwal, M. C. Debnath, and V. Zayets, *Phys. Rev. Lett.* **100**, 067204 (2008).
- ²¹M. Berciu, R. Chakarvorty, Y. Y. Zhou, M. T. Alam, K. Traudt, R. Jakiela, A. Barcz, T. Wojtowicz, X. Liu, J. K. Furdyna, M. Dobrowolska, *Phys. Rev. Lett.* **102**, 247202 (2009).
- ²²G. Acbas, M.-H. Kim, M. Cukr, V. Novak, M. A. Scarpulla, O. D. Dubon, T. Jungwirth, J. Sinova, and J. Cerne, *Phys. Rev. Lett.* **103**, 137201 (2009).
- ²³T. S. Moss, *Proc. Phys. Soc. London, Sect. B* **67**, 775 (1954).
- ²⁴J.-M. Tang and M. E. Flatté, *Phys. Rev. Lett.* **101**, 157203 (2008).
- ²⁵M. Turek, J. Siewert, and J. Fabian, *Phys. Rev. B* **80**, 161201 (2009).
- ²⁶J. Blinowski and P. Kacman, *Phys. Rev. B* **67**, 121204(R) (2003).
- ²⁷K. W. Edmonds, P. Bogusławski, K. Y. Wang, R. P. Campion, S. N. Novikov, N. R. S. Farley, B. L. Gallagher, C. T. Foxon, M. Sawicki, T. Dietl *et al.* *Phys. Rev. Lett.* **92**, 037201 (2004).

- ²⁸L. X. Zhao, C. R. Staddon, K. Y. Wang, K. W. Edmonds, R. P. Campion, B. L. Gallagher, and C. T. Foxon, *Appl. Phys. Lett.* **86**, 071902 (2005).
- ²⁹J. M. Luttinger and W. Kohn, *Phys. Rev.* **97**, 869 (1955).
- ³⁰G. L. Bir and G. E. Pikus, *Symmetry and Strain Induced Effects in Semiconductors* (Wiley, New York, 1974).
- ³¹S. Richard, F. Aniel, and G. Fishman, *Phys. Rev. B* **70**, 235204 (2004).
- ³²S. B. Radhia, N. Fraj, I. Saidi, and K. Boujdaria, *Semicond. Sci. Technol.* **22**, 427 (2007).
- ³³T. Dietl, A. Haury, and Y. M. d'Aubigne, *Phys. Rev. B* **55**, R3347 (1997).
- ³⁴T. Jungwirth, W. A. Atkinson, B. H. Lee, and A. H. MacDonald, *Phys. Rev. B* **59**, 9818 (1999).
- ³⁵T. Dietl, H. Ohno, F. Matsukura, J. Cibert, and D. Ferrand, *Science* **287**, 1019 (2000).
- ³⁶T. Dietl, H. Ohno, and F. Matsukura, *Phys. Rev. B* **63**, 195205 (2001).
- ³⁷J. König, H. H. Lin, and A. H. MacDonald, in *Interacting Electrons in Nanostructures*, edited by R. Haug and H. Schoeller, Lecture Notes in Physics (Springer, Berlin, 2001), Vol. 579.
- ³⁸N. Fraj, S. B. Radhia, and K. Boujdaria, *Solid State Commun.* **142**, 342 (2007).
- ³⁹J. Okabayashi, A. Kimura, O. Rader, T. Mizokawa, A. Fujimori, T. Hayashi, and M. Tanaka, *Phys. Rev. B* **58**, R4211 (1998).
- ⁴⁰J. Szczytko, W. Bardyszewski, and A. Twardowski, *Phys. Rev. B* **64**, 075306 (2001).
- ⁴¹S. C. Jain, J. M. McGregor, and D. J. Roulston, *J. Appl. Phys.* **68**, 3747 (1990).
- ⁴²I. Vurgaftman, J. R. Meyer, and L. R. Ram-Mohan, *J. Appl. Phys.* **89**, 5815 (2001).
- ⁴³M. P. Marder, *Condensed Matter Physics* (Wiley, New York, 2000).
- ⁴⁴S.-R. Eric Yang, J. Sinova, T. Jungwirth, Y. P. Shim, and A. H. MacDonald, *Phys. Rev. B* **67**, 045205 (2003).
- ⁴⁵J. Sinova, T. Jungwirth, J. Kucera, and A. H. MacDonald, *Phys. Rev. B* **67**, 235203 (2003).
- ⁴⁶J. Sinova, T. Jungwirth, S.-R. Eric Yang, J. Kucera, and A. H. MacDonald, *Phys. Rev. B* **66**, 041202 (2002).
- ⁴⁷E. D. Palik, *Handbook of Optical Constants of Solids* (Academic, San Diego, CA, 1998).